Research Square

Preprints are preliminary reports that have not undergone peer review.
They should not be considered conclusive, used to inform clinical practice,
or referenced by the media as validated information.

A GALES--MELTS framework for thermodynamically constrained forward modelling of crystallisation kinetics in magmas

Antonella Longo

antonella.longo@ingv.it

Istituto Nazionale di Geofisica e Vulcanologia Sezione di Pisa https://orcid.org/0000-0001-6590-6346

Deepak Garg

Istituto Nazionale di Geofisica e Vulcanologia

Paolo Papale

Istituto Nazionale di Geofisica e Vulcanologia

Research Article

Keywords: numerical modelling, thermodynamic modeling, crystal nucleation and growth kinetic, melt depletion, experimental petrology, GALES--MELTS interface

Posted Date: November 9th, 2026

DOI: https://doi.org/10.21203/rs.3.rs-11649665/v1

License: This work is licensed under a Creative Commons Attribution 4.0 International License.
Read Full License

Additional Declarations: The authors declare no competing interests.

A GALES–MELTS framework for thermodynamically constrained forward modelling of crystallisation kinetics in magmas

Antonella Longo[1*], Deepak Garg[1] and Paolo Papale[1]

[1]Sede di Pisa, Istituto Nazionale di Geofisica e Vulcanologia, Via Cesare Battisti, 53, Pisa, 56125, Italy.

*Corresponding author(s). E-mail(s): antonella.longo@ingv.it;
Contributing authors: deepak.garg@ingv.it; paolo.papale@ingv.it;

Abstract

Crystallisation controls magma differentiation, rheology and texture, yet its evolution depends on the coupled effects of thermodynamic disequilibrium, nucleation, crystal growth and melt depletion. We present a forward crystallisation framework coupling GALES with alphaMELTS, in which phase affinity and incipient crystal composition are used directly to calculate homogeneous and heterogeneous nucleation and crystal growth. Nucleation follows classical nucleation theory with stochastic crystal births and a kinetic attachment prefactor governed by mixed diffusion- and interface-controlled processes; growth uses an analogous mixed kinetic formulation. Crystallised material is removed explicitly from the liquid, so that residual-melt evolution continuously modifies the thermodynamic driving force.

The framework is tested against two contrasting experiments. For the initially crystal-free Iezzi case (Iezzi et al. 2011), homogeneous nucleation precedes heterogeneous nucleation, and the model reproduces the observed crystallinity, plagioclase composition and main residual-melt differentiation trend. In the slowly cooled Billon G2-2 experiment (Billon et al. 2025), inherited plagioclase provides the substrate for heterogeneous nucleation and no homogeneous nucleation occurs along the modelled cooling path. Retaining the kinetic parameters constrained by Iezzi and recalibrating only the effective heterogeneous nucleation parameters reproduces plagioclase abundance, crystal number density, nucleation rate and residual-glass composition, although the modelled plagioclase remains more sodic than the measured new-growth rims. In both benchmarks, modelled crystal-size distributions remain narrower than observed. Rather than constituting only a model limitation, this mismatch provides an additional constraint

on crystal-population evolution, showing that bulk crystallinity, number density and melt chemistry do not fully determine the textural record. The framework therefore offers a physically based platform for identifying and testing additional processes governing crystal growth and post-nucleation evolution.

Keywords: numerical modelling, thermodynamic modeling, crystal nucleation and growth kinetic, melt depletion, experimental petrology, `GALES`–`MELTS` interface

1 Introduction

The physical and chemical processes governing magmatic crystallisation have been investigated since the foundations of modern igneous petrology (Harker 1909; Bowen 1915, 1928), yet their quantitative description remains a central problem in magma dynamics (Marsh 2007). Crystallisation determines phase abundance, melt differentiation and crystal texture, while the progressive accumulation of crystals modifies magma rheology and therefore influences transport, storage and eruptive behaviour. A predictive treatment must consequently address not only phase stability, but also the rates at which crystals appear and grow as pressure, temperature and melt composition change.

Magmatic crystallisation commonly proceeds away from equilibrium. Homogeneous nucleation can generate crystals in the absence of an effective substrate, whereas heterogeneous nucleation takes place on existing interfaces, including crystal surfaces. Growth then transfers chemical components from the liquid to the solid and changes the composition of the residual melt. The thermodynamic conditions experienced later in the crystallisation history therefore depend partly on the crystallisation that has already occurred. At the same time, undercooling, viscosity, chemical diffusion and interface-attachment kinetics influence the rates of both nucleation and growth. Coarsening, aggregation, Ostwald ripening and morphology-dependent growth may further modify the crystal population after nucleation. Experiments show that these processes act together in controlling crystal abundance, size and morphology (Arzilli and Carroll 2013; Mangler et al. 2023; Welsch et al. 2023; Peres et al. 2024; Billon et al. 2025; Lindoo et al. 2025; Musu et al. 2026).

Different observables preserve different parts of this history. Crystal fraction measures the integrated transfer of mass from liquid to solid, whereas crystal number density is more closely related to the cumulative nucleation history. Residual-melt composition records chemical depletion during crystallisation, and crystal composition constrains the solid phase produced along the evolving thermodynamic path. Crystal-size distributions (CSDs) contain additional information because crystal size depends on both the time of nucleation and the duration and rate of subsequent growth. Interpreting these quantities separately can therefore obscure the coupling among mass transfer, thermodynamic evolution and crystal-population dynamics.

Previous work has addressed these aspects at different levels of complexity. Population-balance theory established the quantitative relationship between CSDs and nucleation and growth histories (Marsh 1988), while stereological approaches

provided methods for reconstructing three-dimensional crystal populations from two-dimensional observations (Higgins 2000). Toramaru (1991) developed an early forward treatment in which homogeneous nucleation, diffusion-limited growth and depletion of the crystallising component evolve together in a simplified system. Experimental studies subsequently quantified the dependence of nucleation and growth on undercooling, time and melt conditions (e.g. Arzilli and Carroll 2013).

Spillar and Dolejš (2013) demonstrated that crystal-size distributions can be inverted to recover time-dependent nucleation and growth rates. Their analysis showed that CSDs alone permit multiple combinations of nucleation and growth histories, whereas combining CSDs with the evolution of crystallinity provides stronger constraints on the kinetic rates. In a subsequent three-dimensional numerical study, Spillar and Dolejš (2015) showed that heterogeneous nucleation can produce crystal clustering, concave-up CSDs and porphyritic or bimodal textures, and may represent the dominant nucleation mechanism in natural magmas. These results emphasise the importance of distinguishing homogeneous from heterogeneous nucleation and of linking crystal-population statistics to the physical processes governing crystallisation.

More recent models have introduced explicit thermodynamic constraints. `SNGPlag` couples `MELTS`-derived equilibrium crystallinity to define a supersaturation measure that drives time-dependent plagioclase nucleation and growth (Andrews and Befus 2020; Marshall and Andrews 2023). Huggins et al. (2021) used `MELTS`-derived chemical affinity to quantify mineral disequilibrium and the tendency for growth or dissolution along evolving P-T-t paths. Lindoo et al. (2025) further emphasised the importance of dynamic undercooling and melt-composition evolution in controlling nucleation, growth and crystal morphology. Table 1 summarises the principal characteristics of these approaches.

A remaining difficulty is to evolve thermodynamics and the crystal population within the same feedback loop. Models based on undercooling or departure from equilibrium crystallinity can reproduce kinetic crystal populations, but the material transferred to the crystals is not always used to update the chemical driving force directly. Conversely, affinity-based calculations quantify instantaneous disequilibrium but do not, by themselves, determine discrete nucleation events and the resulting CSD. A forward crystallisation calculation should therefore allow the current thermodynamic state to determine nucleation and growth, remove the corresponding solid composition from the liquid, and use the depleted melt to determine the next thermodynamic state.

The framework developed here follows this approach by coupling `GALES` (Longo et al. 2012; Garg et al. 2018) with `alphaMELTS` (Smith and Asimow 2005). At each thermodynamic update, `alphaMELTS` supplies phase affinity, incipient solid composition, molar volume and density for the evolving residual liquid. `GALES` uses these quantities to evaluate homogeneous and heterogeneous classical nucleation theory (CNT) rates and crystal growth. In the nucleation rate, the CNT free-energy barrier is combined with an attachment prefactor governed by mixed diffusion- and interface-controlled kinetics; the growth coefficient is treated with an analogous mixed kinetic formulation. Individual nucleation events are sampled stochastically. Crystal growth then removes mass from the melt according to the instantaneous solid composition predicted by

`alphaMELTS`, after which the modified liquid is returned to the thermodynamic calculation. Thermodynamic driving force, nucleation, growth, crystal population and melt chemistry consequently evolve together rather than being prescribed independently. This is the central feedback implemented in the model.

Two experimental datasets are used to examine different crystallisation regimes. The Iezzi et al. (2011) experiments begin from a strongly superheated, initially crystal-free andesitic melt and provide the principal constraint on homogeneous nucleation and growth, followed by heterogeneous nucleation once crystal surfaces develop. The Billon et al. (2025) G2-2 experiment starts instead with inherited plagioclase crystals and proceeds at a much lower cooling rate. In that case homogeneous nucleation does not occur along the modelled cooling path; new crystals are produced by heterogeneous nucleation on the available plagioclase surfaces. The kinetic parameters constrained with Iezzi are retained, whereas recalibration for Billon is restricted to the effective heterogeneous nucleation parameters. Phase abundance, crystal number density, residual-melt composition, crystal composition and CSD are compared with the experiments so that thermodynamic, kinetic and population-scale behaviour are tested independently.

The paper is organised as follows. Section 2 presents the coupled `GALES`–`alphaMELTS` formulation. Section 3 describes the feedbacks between nucleation, growth, melt depletion, and thermodynamic evolution, while Section 4 introduces the observables used to constrain the model. Section 5 compares the calculations with the Iezzi et al. (2011) and Billon et al. (2025) experiments. Sections 6 and 7 present the discussion and conclusions, respectively.

Table 1: Selected approaches to the analysis and modelling of crystallisation kinetics in magmatic systems. The studies have different objectives and are not intended as directly competing models.

Study	**Approach**	**Thermodynamic driving force**	**Nucleation and growth**	**Crystal population and melt feedback**
Marsh (1988)	CSD population-balance theory	Not explicitly calculated	Nucleation and growth rates inferred from CSD characteristics	CSD provides information on crystal number, size, growth history and crystallisation timescale; no explicit melt-composition evolution.
Toramaru (1991)	Forward kinetic crystallisation model	Undercooling in a simplified two-component system	Homogeneous nucleation and diffusion-limited growth	Crystal number and mean size evolve dynamically; depletion of the crystallising component feeds back on supersaturation.
Spillar and Dolejš (2013)	CSD inversion for time-dependent kinetics	Not explicitly calculated; crystallinity evolution used as an additional constraint	Nucleation and growth rates inferred from CSDs and crystallinity evolution	CSD and crystallinity constrain the reconstructed kinetic history; no explicit thermodynamic or residual-melt feedback.

Continued on next page

Table 1 – continued from previous page

Study	Approach	Thermodynamic driving force	Nucleation and growth	Crystal population and melt feedback
Spillar and Dolejš (2015)	Three-dimensional numerical model of magmatic textures	Gibbs free energy of crystallisation; heterogeneous nucleation lowers the nucleation-energy barrier	Homogeneous and heterogeneous nucleation with crystal growth; heterogeneous nucleation progressively increases with the prescribed heterogeneous-nuclei fraction	Crystal textures, CSD curvature and clustering evolve explicitly; static melt composition and thermodynamic conditions, with no residual-melt depletion feedback.
Higgins (2000)	CSD measurement and stereological reconstruction	—	—	Conversion of two-dimensional crystal measurements to three-dimensional CSDs, accounting for crystal shape and fabric.
Andrews and Befus (2020)	SNGPlag forward model	`MELTS`-derived equilibrium crystallinity and supersaturation $\Delta\phi_{\mathrm{plag}}$	Time-dependent nucleation and growth parameterised as functions of $\Delta\phi_{\mathrm{plag}}$	Explicit crystallinity, crystal number density and CSD; kinetic crystallisation reduces the departure from equilibrium crystallinity.
Huggins et al. (2021)	Affinity-based disequilibrium model	`MELTS`-derived chemical affinity	Affinity used to evaluate crystal growth or dissolution tendency; nucleation is not explicitly resolved	No explicit crystal-population evolution or residual-melt depletion; focus on thermodynamic disequilibrium along P–T–t paths.

Continued on next page

Table 1 – continued from previous page

Study	Approach	Thermodynamic driving force	Nucleation and growth	Crystal population and melt feedback
Marshall and Andrews (2023)	SNGPlag applied to basaltic andesite	`MELTS`-derived $\Delta\phi_{\text{plag}}$	Experimentally calibrated nucleation and growth laws	Explicit CSD and crystal-population evolution used to constrain decompression histories.
Lindoo et al. (2025)	Forward nucleation–growth model and experiments	`MELTS`-derived saturation and dynamically evolving instantaneous undercooling	Time-dependent nucleation and growth, including nucleation delay	Melt-composition evolution and polydisperse crystal populations are represented; emphasis on dynamic undercooling and crystal morphology.
This study	Coupled `GALES`–`MELTS` forward model	Instantaneous `MELTS` phase affinity and incipient phase composition	Homogeneous and heterogeneous CNT nucleation with stochastic births; mixed diffusion/interface-controlled attachment for nucleation and growth	Explicit CSD and crystal population; phase-specific mass removal updates the residual melt, which modifies subsequent affinity, nucleation, growth and phase composition.

2 Methods

The crystallisation model couples the kinetic framework implemented in `GALES` with thermodynamic calculations performed by `alphaMELTS` (Smith and Asimow 2005), as schematically illustrated in Figure 1. `GALES` resolves the time-dependent evolution of the crystal population through nucleation and growth, together with the progressive depletion of the residual melt, whereas `alphaMELTS` provides the thermodynamic properties of the incipient crystalline phases. The state of the system is described by temperature T, pressure P, residual-liquid composition X_i, solid composition Y_i, and crystal population N_i. At time t_n, the system is represented by

$$\left\{T^n,\, P^n,\, X_i^n,\, Y_i^{n-1},\, N_i^{n-1}\right\}.$$

At each thermodynamic update, the subset

$$\{T^n,\, P^n,\, X_i^n\}$$

is supplied to `alphaMELTS`, which evaluates the metastable thermodynamic state of the system and returns, for each potentially crystallising phase, the phase affinity A_i, incipient solid composition Y_i^n, molar volume $V_{m,i}$, and density ρ_i. These thermodynamic quantities are then transferred to `GALES` and used to evaluate the nucleation rate J_i^n and crystal growth rate G_i^n. The crystal population is consequently updated from N_i^{n-1} to N_i^n. The mass crystallised during the timestep is removed from the residual liquid according to the incipient solid composition predicted by `alphaMELTS`, yielding the updated liquid composition X_i^{n+1}, while the corresponding material is added to the solid phase Y_i^n. The updated thermodynamic state is then used as the initial condition for the following timestep t_{n+1}.

`GALES` and `alphaMELTS` communicate through a persistent TCP/IP client–server interface. At each thermodynamic update, `GALES` sends the current temperature, pressure, and residual-liquid composition to `alphaMELTS`, which returns the phase properties required by the kinetic model. This coupling allows the thermodynamic driving force, phase composition, nucleation, crystal growth, and melt depletion to evolve consistently throughout the crystallisation history.

Both nucleation and crystal growth are controlled by the thermodynamic driving force derived from the `alphaMELTS` phase affinity and by kinetic attachment processes. In the present formulation, attachment is described using a mixed diffusion- and interface-controlled mechanism, in which the two kinetic contributions act as resistances in series.

For the Iezzi et al. benchmark, thermodynamic calculations were performed using the standard `MELTS` thermodynamic model (Ghiorso and Sack 1995; Asimow and Ghiorso 1998), while for the Billon et al. benchmark, thermodynamic calculations were performed using `Rhyolite-MELTS 1.2.0` (Gualda et al. 2012; Ghiorso and Gualda 2015), both through the `alphaMELTS` interface (Smith and Asimow 2005).

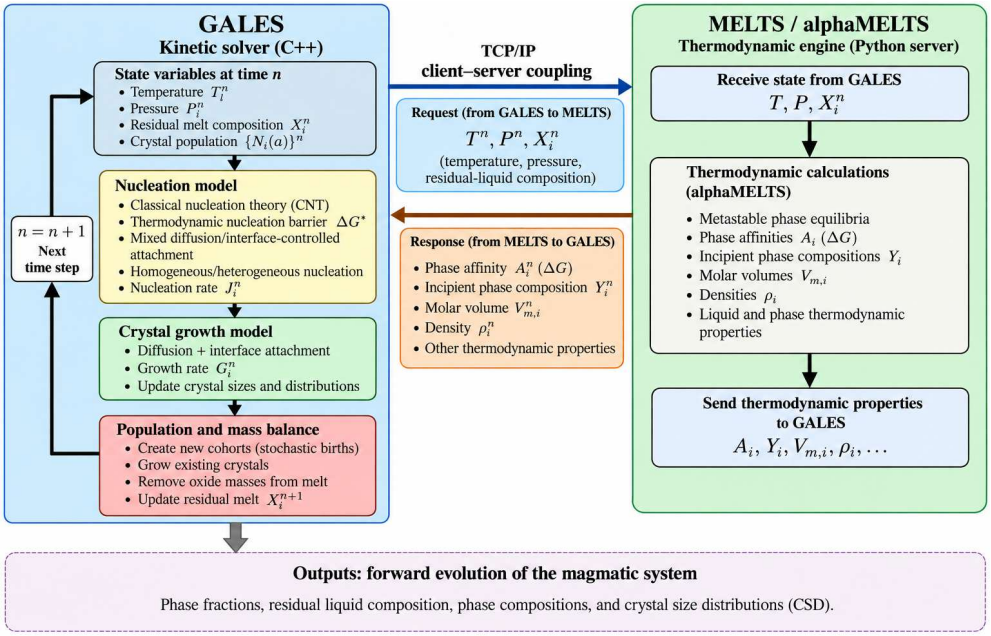


Fig. 1 Schematic representation of the `GALES`–`alphaMELTS` coupling. At each thermodynamic update, temperature, pressure, and residual-liquid composition are transferred from `GALES` to `alphaMELTS`. `alphaMELTS` returns the affinity, composition, molar volume, and density of the incipient crystalline phases. These quantities determine the nucleation and growth rates in `GALES`, which update the crystal population and the mass transferred from the melt to the solid. The resulting residual-liquid composition is then used for the subsequent thermodynamic update.

Nucleation is controlled by a CNT free-energy barrier determined by the thermodynamic driving force and crystal–liquid interfacial energy, whereas both nucleation and growth depend on mixed diffusion- and interface-controlled attachment kinetics.

2.1 Nucleation rates

Nucleation is represented through both homogeneous and heterogeneous mechanisms. Homogeneous nucleation provides the reference CNT mechanism in the absence of an effective substrate, whereas heterogeneous nucleation occurs on pre-existing surfaces and generally involves a reduced nucleation barrier. In the present model, such surfaces may either be inherited from the initial condition, as in the Billon et al. experiments, or generated dynamically by crystals formed during the simulation. Both mechanisms share the same mixed diffusion/interface-controlled attachment kinetics, while heterogeneous nucleation differs through an effective reduction of the CNT barrier and its dependence on the available crystal surface area.

The nucleation barrier depends on the magnitude of the thermodynamic driving force derived from the `alphaMELTS` affinity A and the molar volume V_m. For CNT calculations, the volumetric driving-force magnitude is defined as:

$$\Delta G_v^{\mathrm{CNT}} = \frac{|A|}{V_m}. \tag{1}$$

2.1.1 Homogeneous nucleation rate

Classical nucleation theory describes crystal formation as the competition between the volumetric thermodynamic driving force for crystallisation and the energetic cost associated with formation of a crystal–liquid interface (Turnbull and Fisher 1949; Kashchiev 2000; Kelton and Greer 2010). This framework has been extensively applied to nucleation in silicate melts and glasses (Hammer 2004; Fokin et al. 2006).

Following classical nucleation theory, the steady-state homogeneous nucleation rate is written as (Turnbull and Fisher 1949; Kashchiev 2000; Kelton and Greer 2010):

$$J_{\mathrm{hom}} = N_0 Z f^+ \exp\left(-\frac{\Delta G^*_{\mathrm{hom}}}{k_{\mathrm{B}} T}\right) \tag{2}$$

where $N_0 = N_{\mathrm{A}}/V_m$ is the number density of potential nucleation sites, N_{A} is the Avogadro number, Z is the Zeldovich factor, and f^+ is the attachment frequency at the critical nucleus. $\Delta G^*_{\mathrm{hom}}$ is the Gibbs free-energy barrier associated with the formation of a critical nucleus with critical radius:

$$r^* = \frac{2\gamma}{\Delta G_v^{\mathrm{CNT}}}. \tag{3}$$

The homogeneous nucleation barrier is thus:

$$\Delta G^*_{\mathrm{hom}} = \frac{16\pi\gamma^3}{3(\Delta G_v^{\mathrm{CNT}})^2}. \tag{4}$$

where γ is the liquid–crystal interfacial energy.

Since $\Delta G^*_{\mathrm{hom}}$ contains the cubic γ and the inverse square of affinity, and since $\Delta G^*_{\mathrm{hom}}$ appears inside the exponential function, the dependence of nucleation rate on the interfacial energy and affinity is critical. Even small changes in γ and A may lead to enormous changes in J.

The Zeldovich factor Z is:

$$Z = \sqrt{\frac{\Delta\mu}{6\pi k_{\mathrm{B}} T n^*}} \tag{5}$$

where $\Delta\mu = |A|/N_{\mathrm{A}}$, and $n^* = (4/3\pi(r^*)^3/v_0)$ with $v_0 = v_m/N_{\mathrm{A}}$ is the number of structural units in the critical nucleus.

Crystal attachment can be limited either by transport through the liquid or by reactions at the crystal–melt interface, with their relative importance varying with temperature, undercooling and melt properties (Kirkpatrick 1975, 1981; Muncill and Lasaga 1988).

The mixed diffusion/interface attachment frequency to critical nucleus f^+ is thus:

$$f^+ = \frac{4\pi(r^*)^2}{a^3_{\mathrm{nuc}}} k_{\mathrm{eff,nuc}} \tag{6}$$

where:

$$a_{\mathrm{nuc}} = \left(\frac{v_m}{N_{\mathrm{A}}}\right)^{1/3} \tag{7}$$

is the characteristic molecular length for nucleation or nucleation structural-unit length.

$k_{\mathrm{eff,nuc}}$ is the coefficient representative of the mixed contributions of diffusion $k_{\mathrm{diff,nuc}}$ and interface-controlled regime $k_{\mathrm{int,nuc}}$. Here, the two contributions are represented as sequential kinetic resistances:

$$\frac{1}{k_{\mathrm{eff,nuc}}} = \frac{1}{k_{\mathrm{diff,nuc}}} + \frac{1}{k_{\mathrm{int,nuc}}}. \tag{8}$$

The diffusion attachment coefficient $k_{\mathrm{diff,nuc}}$ is:

$$k_{\mathrm{diff,nuc}} = \frac{D}{a_{\mathrm{nuc}}} \tag{9}$$

The diffusivity of structural units in the melt D is estimated from the Stokes–Einstein relation (Einstein 1905; Sutherland 1905), which provides an approximate connection between molecular mobility and melt viscosity:

$$D = \frac{k_{\mathrm{B}}T}{6\pi\eta a_{\mathrm{nuc}}} \tag{10}$$

where η is the melt viscosity, calculated following Giordano et al. (2008), and a_{nuc} is the characteristic length scale associated with the diffusing structural unit. The use of the Stokes–Einstein relation at molecular scales in multicomponent silicate melts represents an effective approximation of transport kinetics (e.g. Mungall 2002).

The interface-controlled attachment coefficient $k_{\mathrm{int,nuc}}$ is:

$$k_{\mathrm{int,nuc}} = a_{\mathrm{nuc}}\,\nu_{\mathrm{nuc}} \exp\left(-\frac{Q_{\mathrm{nuc}}}{RT}\right) \tag{11}$$

where ν_{nuc} represents the characteristic frequency at which structural units at the melt-nucleus interface attempt to cross/attach to the crystalline structure, while the Arrhenius term $\exp(-Q_{\mathrm{nuc}}/RT)$ gives the fraction of those attempts that can overcome the interface-attachment activation barrier.

2.1.2 Heterogeneous nucleation rate

Heterogeneous nucleation is represented through the classical reduction of the nucleation barrier produced by a pre-existing substrate (Turnbull 1950; Fletcher 1958; Kelton and Greer 2010). In the present formulation this effect is represented by an effective barrier-reduction factor ϕ_{het},

$$\Delta G^*_{\mathrm{het}} = \phi_{\mathrm{het}} \Delta G^*_{\mathrm{hom}} \tag{12}$$

The heterogeneous nucleation rate reads:

$$J_{\mathrm{het}} = N_s Z f^+ \exp\left(-\frac{\Delta G^*_{\mathrm{het}}}{k_{\mathrm{B}}T}\right) \tag{13}$$

where Z and f^+ are expressed as in the homogeneous nucleation rate (Eqs. (5) and (6)). In particular, the attachment frequency f^+ is governed by mixed diffusion/interface-controlled kinetics. Unlike the homogeneous case, the density of active sites N_s (*vs* N_0 in homogeneous nucleation) is the density of active sites on the existing crystal surface:

$$N_s = \frac{f_{\text{site}}}{a_{\text{nuc}}^2} \tag{14}$$

where f_{site} is the active-site fraction.

Therefore, f_{site} controls how many sites can nucleate, while ϕ_{het} controls how easy nucleation is at those sites.

2.1.3 Distribution of new nuclei

The nucleation rates derived above define the expected frequency of nucleation events, but they do not imply that a deterministic, non-integer number of crystals forms during each timestep. Nucleation is instead a discrete stochastic process: individual nuclei appear as separate events, and even under identical thermodynamic conditions the exact number formed during a finite time interval may vary between otherwise equivalent realisations. The model therefore converts the continuous nucleation rate into an integer number of newly formed nuclei through Poisson sampling.

For homogeneous and heterogeneous nucleation, the expected number of events in an element during one timestep is given by:

$$\lambda_{\text{hom}} = J_{\text{hom}} V \Delta t \tag{15}$$

$$\lambda_{\text{het}} = J_{\text{het}} A_{\text{het}} \Delta t \tag{16}$$

since the homogeneous nucleation rate states how many crystals form per unit volume V, while heterogeneous nucleation deals with nucleation per available unit area A_{het}.

The quantity λ is therefore the mean number of nucleation events expected within the considered spatial region and timestep. The realised number of physical nuclei is sampled from a Poisson distribution,

$$N_{\text{nuc}} \sim \text{Poisson}(\lambda), \tag{17}$$

with probability mass function

$$P(N_{\text{nuc}} = k) = \frac{\lambda^k e^{-\lambda}}{k!}, \qquad k = 0, 1, 2, \ldots. \tag{18}$$

The Poisson distribution is appropriate because nucleation is represented as a sequence of discrete events occurring with a locally defined mean rate. Over a sufficiently short timestep, the thermodynamic and kinetic state of an individual finite element can be regarded as approximately constant, so that the probability of a nucleation event is governed by the instantaneous nucleation rate. In addition, nucleation events are treated as statistically independent over that interval, conditional on the

current thermodynamic state and available substrate. Under these assumptions, the number of events occurring within a fixed space–time interval follows a Poisson process.

This formulation has several useful properties. First, the expected value of the sampled number is

$$\mathbb{E}[N_{\mathrm{nuc}}] = \lambda, \tag{19}$$

so that the deterministic CNT nucleation rate is recovered when many statistically independent realisations are averaged. The variance is also

$$\mathrm{Var}(N_{\mathrm{nuc}}) = \lambda, \tag{20}$$

which introduces the physically expected fluctuations in the number of nuclei produced during finite intervals. When $\lambda \ll 1$, most timesteps generate no nucleus and occasional timesteps generate one, reproducing the intermittent character expected when nucleation is rare. As λ increases, multiple nuclei can form within the same timestep and the relative magnitude of the stochastic fluctuations decreases approximately as $1/\sqrt{\lambda}$.

The Poisson treatment therefore separates two aspects of the model: CNT and the attachment kinetics determine the expected nucleation intensity λ, whereas stochastic sampling determines the particular integer number of crystals realised in an individual simulation. Different random-number seeds consequently produce slightly different crystal populations even when all thermodynamic and kinetic parameters are identical, while the ensemble-averaged population converges toward that predicted by the underlying nucleation rate.

2.2 Growth rate

The thermodynamic dependence of the growth rate is expressed through an affinity term consistent with transition-state/irreversible thermodynamic descriptions of mineral reaction kinetics (Lasaga 1981, 1998), while the kinetic coefficient accounts for transport and crystal–melt interface attachment (Kirkpatrick 1981; Muncill and Lasaga 1988):

$$G = k_{\mathrm{eff,grow}} \left[1 - \exp\left(\frac{A}{RT}\right)\right] \tag{21}$$

where $k_{\mathrm{eff,grow}}$, $k_{\mathrm{diff,grow}}$ and $k_{\mathrm{int,grow}}$ are analogous to the nucleation rate ones (Eqs. 9- 11), but with appropriate coefficients a_{grow}, ν_{grow} and Q_{grow} representative of macroscopic crystal growth.

The increase in crystal radius during one timestep is:

$$\Delta R = G\Delta t \tag{22}$$

2.3 Probabilistic ensemble

Because crystal nucleation is treated stochastically, the calibrated simulation was repeated for 20 independent random-number seeds. All thermodynamic, kinetic, and numerical parameters were kept identical among realisations, so that differences

between runs reflect only the stochastic sampling of homogeneous and heterogeneous nucleation events. Ensemble means and sample standard deviations were calculated for the principal model outputs, including phase fractions, crystal population, nucleation temperatures, phase compositions, residual-liquid chemistry, and crystal-size distributions. The ensemble therefore provides a test of whether model–experiment agreement is a robust consequence of the calibrated physical formulation or depends on a particular stochastic realisation.

AI use statement

Large language models (LLMs) were used for AI-assisted copy editing of author-generated text, including checks for grammar, spelling, punctuation, and tone. LLMs were also used to assist in digitising crystal-size distribution (CSD) data from published figures in Iezzi et al. (2011). All scientific reasoning, model development, numerical analysis, interpretation, and conclusions were performed and verified by the authors, and the digitised CSD data were checked against the original publications.

3 Feedback during crystal evolution

Crystallisation in the present model results from the continuous coupling between thermodynamic driving force, nucleation, crystal growth, and the progressive evolution of the residual melt. Thermodynamics determines whether crystallisation is favorable, the magnitude of the driving force, and the composition of the incipient solid phase. The actual mass transferred from liquid to crystals during a timestep is then determined kinetically through the combined effects of nucleation and growth.

The crystallised mass and crystal population are therefore dynamically coupled. An increase in nucleation rate J produces a larger number of crystals per unit volume, N_V, and consequently a larger population of crystals available for subsequent growth. Conversely, a lower nucleation rate generates a smaller crystal population. Because all crystals draw material from the same evolving residual melt, changes in the number of nuclei modify how the crystallised material is distributed among individual crystals. A high nucleation rate tends to divide the available crystallised mass among many crystals, whereas a low nucleation rate concentrates the transferred mass into a smaller number of growing crystals. As a consequence, high nucleation rates produce more abundant smaller crystals, while low nucleation rates generate less abundant larger crystals.

Nucleation is also coupled to the evolving thermodynamic state of the melt through the thermodynamic driving force. Once nucleation begins, the newly formed crystals subsequently grow and remove from the liquid the components required by the incipient solid phase. This progressive chemical depletion modifies the residual-melt composition and, consequently, the affinity of the phase during subsequent timesteps. In the adopted convention, crystallisation is favoured for negative affinity; therefore, as crystallisation proceeds, the affinity generally shifts toward less negative values and may eventually approach zero or become positive. The corresponding decrease in supersaturation reduces the volumetric driving force for crystallisation, which increases the critical nucleation barrier and suppresses the nucleation rate. At the same time,

the reduced thermodynamic driving force also decreases the crystal growth rate. Crystallisation therefore generates a negative feedback on its own kinetics: nucleation and growth progressively modify and deplete the residual melt, reducing the thermodynamic driving force for further nucleation and growth. This feedback contributes to the self-limiting evolution of the crystal population and couples the instantaneous kinetic response to the preceding crystallisation history.

The progressive increase in crystal surface area promotes heterogeneous nucleation by providing additional substrate and increases the total crystal–melt interface available for growth. This produces a positive kinetic feedback: as crystals grow and new crystals form, the available surface area increases, promoting further heterogeneous nucleation and increasing the total growth capacity of the crystal population. The linear growth rate of an individual crystal, however, remains controlled by the local thermodynamic and kinetic conditions. At the same time, crystallisation removes oxide components from the melt and drives the phase affinity toward less negative values, reducing the thermodynamic driving force and ultimately suppressing both nucleation and growth.

An additional feedback arises when more than one crystalline phase forms from the same melt. Because all phases draw their components from a common residual liquid, crystallisation of one phase modifies the melt composition experienced by the others. This compositional change alters their thermodynamic affinities and therefore their subsequent nucleation and growth rates. As a consequence, the evolution of each phase is not independent: crystallisation of one phase can either promote or suppress the crystallisation of another, depending on how the shared melt composition is modified. The interaction is reciprocal, so the development of one crystalline population can influence the thermodynamic and kinetic evolution of the others, and vice versa.

In cooling-induced crystallisation, the evolution of the nucleation rate reflects the competition between two opposing effects. Progressive cooling generally increases supersaturation and strengthens the thermodynamic driving force for crystallisation, thereby promoting nucleation. At the same time, nucleation and subsequent crystal growth remove from the melt the components incorporated into the crystallising phase. This compositional depletion shifts the phase affinity toward less negative values, reducing the thermodynamic driving force and consequently suppressing further nucleation. The resulting nucleation history therefore emerges from the balance between the positive effect of continued cooling and the negative feedback associated with progressive melt depletion.

The simulations show that homogeneous nucleation does not begin immediately at the `MELTS` saturation temperature, but only after a finite degree of undercooling has developed. During this interval, the affinity becomes progressively more negative and the magnitude of the thermodynamic driving force increases. Consequently, the critical nucleation barrier decreases, leading to a rapid increase in the homogeneous nucleation rate once nucleation becomes kinetically accessible. This produces a short nucleation burst rather than an immediate response at the saturation temperature. The resulting increase in crystal number, followed by rapid crystal growth, enhances the removal of the incipient-phase components from the melt. The associated compositional depletion shifts the affinity back toward less negative values, reduces the

thermodynamic driving force, increases the nucleation barrier, and therefore rapidly suppresses further nucleation. Homogeneous nucleation thus exhibits a self-limiting feedback: undercooling initially strengthens the driving force and triggers a nucleation burst, whereas the crystallisation induced by that burst progressively modifies the melt and inhibits subsequent nucleation.

The strong coupling among thermodynamic driving force, nucleation, crystal growth, melt depletion, and the evolving crystal surface area makes direct calibration of the complete model against a laboratory experiment inherently non-trivial. Because several parameters influence different, and sometimes overlapping, aspects of the crystallisation history, a hierarchical calibration strategy is more appropriate than attempting to constrain all parameters simultaneously. The model is therefore calibrated incrementally against progressively more complex subproblems: homogeneous nucleation is constrained first, followed by crystal growth and, where relevant, heterogeneous nucleation and multiphase interactions. This stepwise procedure allows the contribution of each kinetic process to be isolated as far as possible and provides a clearer connection between individual model parameters and the experimental observables used to constrain them.

4 Constraining variables

The experimental observables used to evaluate and calibrate the model constrain different components of the coupled thermodynamic–kinetic formulation. No single observable uniquely determines one model parameter; rather, the simultaneous reproduction of several independent quantities progressively restricts the range of physically acceptable model behaviour. The principal constraining variables considered here are:

- saturation temperature;
- nucleation temperature;
- crystal volume fraction;
- crystal number density;
- residual-melt composition;
- crystal composition;
- crystal-size distribution.

The saturation temperature primarily constrains the thermodynamic description of phase stability. It corresponds to the conditions at which the thermodynamic driving force for formation of a given phase emerges, i.e. where its affinity approaches zero and changes sign. The interfacial energy γ does not determine the thermodynamic saturation temperature. Instead, through its contribution to the classical nucleation barrier, it controls the degree of undercooling required before nucleation becomes kinetically significant. Consequently, the difference between the thermodynamic saturation temperature and the temperature at which crystals actually begin to nucleate provides a constraint on the kinetic nucleation formulation, particularly on γ, Q_{nuc}, and the associated attachment kinetics.

The final crystal volume fraction, ϕ, primarily constrains the integrated mass transfer from liquid to solid produced by nucleation and growth over the entire crystallisation history. It does not uniquely constrain the number of crystals involved in that transfer. Two simulations may therefore produce similar final crystal fractions while generating very different crystal number densities and characteristic crystal sizes.

The crystal number density, N_{V}, provides a more direct constraint on the integrated nucleation history. It records the total number of crystals generated per unit volume and is therefore sensitive to the magnitude and duration of the nucleation rate. In the present formulation it consequently constrains parameters controlling homogeneous and heterogeneous nucleation, including γ, Q_{nuc}, ϕ_{het}, and f_{site}, depending on the dominant nucleation mechanism. Nevertheless, N_{V} contains limited information about when individual crystals formed: similar final number densities can result from different temporal nucleation histories.

The residual-melt composition provides an independent constraint on the mass-balance and thermodynamic evolution of the coupled system. Because crystals continuously remove oxide components from the liquid according to the incipient phase compositions returned by `alphaMELTS`, the final melt composition integrates both the total amount of crystallisation and the chemical composition of the material transferred to the solid throughout the cooling history. Agreement with the experimentally measured residual glass therefore tests whether the model correctly reproduces the cumulative chemical depletion of the melt and its feedback on phase affinity and subsequent crystallisation. It is not primarily a constraint on crystal number: substantially different nucleation histories may produce similar residual-melt compositions if they result in comparable total mass and chemical partitioning into the crystalline phases.

The crystal composition provides a complementary constraint on the thermodynamic description of the solid phase. At each thermodynamic update, `alphaMELTS` determines the composition of the incipient crystal in equilibrium with the instantaneous residual melt. Comparison with measured crystal compositions therefore tests whether the model correctly predicts the chemical partitioning between melt and crystal along the evolving thermodynamic trajectory. In particular, comparison with experimentally measured crystal rims provides a constraint on the instantaneous composition of newly formed or growing crystal material. A systematic mismatch in crystal composition despite agreement in residual-melt composition may therefore indicate limitations in the thermodynamic prediction of the solid composition or kinetic disequilibrium during crystal growth, rather than an incorrect melt-evolution path alone. This distinction is illustrated by the Billon benchmark, where the modelled residual glass agrees closely with the experiment whereas the modelled plagioclase remains systematically more sodic than the measured rims.

The crystal-size distribution (CSD) provides the most integrated constraint because it records the combined effects of nucleation timing and subsequent crystal growth. Crystals that nucleate early experience a longer interval of growth and can populate the large-size tail of the distribution, whereas crystals nucleated later remain comparatively small. A narrow nucleation interval therefore tends to generate a narrower range of growth durations, whereas a broader nucleation history may generate a wider CSD.

Consequently,

T_{sat}→thermodynamic phase stability,
$T_{\mathrm{sat}} - T_{\mathrm{nuc}}$→kinetic nucleation barrier and attachment kinetics,
ϕ→integrated crystallised mass,
N_{V}→integrated nucleation history,
X_{melt}→mass balance and residual-melt thermodynamic trajectory,
Y_{crystal}→thermodynamic phase composition and possible kinetic disequilibrium,
CSD→combined temporal history of nucleation and growth.

These observables are therefore complementary. Agreement in crystal fraction alone does not demonstrate that nucleation is correctly reproduced, because the same crystallised mass can be distributed among very different numbers of crystals. Similarly, agreement in both ϕ and N_{V} does not guarantee reproduction of the observed CSD, because the timing of nucleation and subsequent growth histories may still differ. Residual-melt and crystal compositions add independent chemical constraints: the former tests the integrated chemical depletion and mass balance of the evolving melt, whereas the latter tests the composition of the solid predicted along that thermodynamic trajectory. Simultaneous comparison of phase abundance, crystal number density, melt and crystal compositions, and CSD therefore provides a progressively more stringent test of the coupled thermodynamic and kinetic description of crystallisation.

5 Test against laboratory experiments

The crystallisation model was tested against two independent experimental datasets characterised by well-controlled and complementary initial and thermal conditions. The experiments of Iezzi et al. (2011) and Billon et al. (2025) were selected because they are nominally anhydrous, thereby avoiding the additional complexity introduced by dissolved H_2O, which strongly affects phase stability, melt viscosity, diffusivity, and therefore both nucleation and growth kinetics. They also provide the main observables required for a comprehensive model comparison, including crystallinity, crystal number density, nucleation behaviour, residual-melt composition, crystal composition, and crystal-size distribution.

The experiments of Iezzi et al. (2011) represent dynamic crystallisation from an initially crystal-free and strongly superheated andesitic melt. The starting material was held well above the liquidus before cooling, and the experiments showed that plagioclase and Fe–Ti oxides initially nucleated homogeneously, followed by heterogeneous nucleation as crystallisation progressed. In contrast, the Billon et al. (2025) experiments started from a melt containing a statistically significant population of inherited plagioclase seeds after the 1190 °C pre-treatment and were subsequently cooled at only 3 °C h^{-1}, providing a complementary test dominated by crystal growth and heterogeneous nucleation on pre-existing surfaces.

The Iezzi et al. experiment was used as the primary calibration benchmark for the homogeneous nucleation and growth formulation, together with the effective heterogeneous nucleation parameters appropriate to an initially crystal-free melt. The Billon et al. experiment was subsequently used to test the transferability of the kinetic parameters constrained against Iezzi under a contrasting, inherited-seed-dominated initial condition. The CNT attachment and growth parameters calibrated against Iezzi et al. were retained unchanged, whereas recalibration was restricted to the two effective heterogeneous nucleation parameters, ϕ_{het} and f_{site}. No homogeneous nucleation occurred during the modelled Billon cooling path.

Other crystallisation experiments were not selected for this first validation because many involve hydrous or decompression conditions, introducing additional coupling among volatile solubility, exsolution, phase stability and transport properties, or because they do not provide the same complete set of observables needed to constrain the different components of the model simultaneously.

5.1 Iezzi et al. experiment

The Iezzi et al. experiment is particularly suitable for constraining the onset of homogeneous nucleation because cooling starts from a strongly superheated, initially crystal-free melt, with no experimental evidence for preferential nucleation on the container walls or bubble surfaces. It therefore provides a suitable benchmark for the transition from primary homogeneous nucleation to subsequent heterogeneous nucleation on newly formed crystal surfaces. The 0.5 °C/min, 1100 °C experiment is selected because it provides a comparatively simple crystallisation regime dominated by plagioclase and Fe–Ti oxides in a residual glass, before the appearance of clinopyroxene and the stronger intergrowth/coarsening observed at lower temperatures. Faster cooling experiments are more strongly affected by disequilibrium crystallisation, whereas slower cooling and lower-temperature runs involve increasingly important coarsening and multiphase interactions not represented in the present model.

The interaction between plagioclase and Fe–Ti oxides requires separate modelling of nucleation and growth for each phase. Plagioclase is allowed to nucleate both homogeneously and heterogeneously, while Fe–Ti oxides have only homogeneous nucleation. Although Iezzi et al. also report a transition from homogeneous to heterogeneous nucleation for Fe–Ti oxides, heterogeneous oxide nucleation is not explicitly represented here. Because Fe–Ti oxides constitute only a minor crystalline fraction in the selected 1100 °C benchmark, their treatment is restricted to the primary homogeneous-nucleation stage, while the heterogeneous nucleation formulation is constrained using the much larger plagioclase population.

The calibration was performed hierarchically, with different parameters constrained primarily by different experimental observables rather than by a simultaneous unconstrained fit of all parameters. Table 2 reports the best values of the parameters describing the nucleation and growth rates. The plagioclase interfacial energy $\gamma_{\mathrm{plag}} = 0.0445$ J m^{-2} was selected from sensitivity tests to obtain a homogeneous nucleation intensity and crystal population compatible with the 1100 °C Iezzi experiment. Because the CNT barrier depends on γ^3, this parameter mainly controlled

the onset and magnitude of primary homogeneous nucleation. The nucleation activation energy $Q_{\mathrm{nuc}} = 285$ kJ mol^{-1} was subsequently retained to preserve this homogeneous-nucleation benchmark, whereas the growth activation energy Q_{growth} was tested independently to control the integrated post-nucleation growth, with crystal size, CSD position and final plagioclase fraction used as the principal constraints. Tests with lower Q_{growth} values modified growth rates but did not recover the experimentally observed large-crystal tail, and the baseline value of 285 kJ mol^{-1} was therefore retained. For Fe–Ti oxides, the interfacial energy $\gamma_{\mathrm{FeTi}} = 0.46$ J m^{-2} was used to regulate homogeneous oxide nucleation and to obtain the minor Fe–Ti abundance observed at the 1100 °C endpoint. In contrast, $Q_{\mathrm{FeTi}} = 267$ kJ mol^{-1} should not be regarded as an independently fitted experimental parameter; it was chosen as a first physically motivated sensitivity value such that interface and diffusion attachment rates were comparable near the modelled Fe–Ti nucleation onset.

Once the homogeneous nucleation and growth parameters were fixed, the heterogeneous plagioclase parameters were calibrated against the experimentally inferred transition from homogeneous to heterogeneous nucleation and against the resulting crystal population. The barrier reduction factor ϕ_{het} controlled whether heterogeneous nucleation could develop without overwhelming the primary homogeneous population. Values substantially below 0.60 produced excessive or runaway heterogeneous nucleation, whereas $\phi_{\mathrm{het}} = 0.6$ preserved the homogeneous-first sequence and the experimentally consistent total crystallinity. At fixed ϕ_{het}, the active-site fraction f_{site} primarily controlled the relative number of secondary heterogeneous nuclei. The adopted value $f_{\mathrm{site}} = 0.003$ increased the heterogeneous contribution while retaining the bulk crystal fraction and provided the lowest CSD shape error among the tested $\phi_{\mathrm{het}} = 0.6$ cases. The final homogeneous and heterogeneous rates are reported in Figure 2.

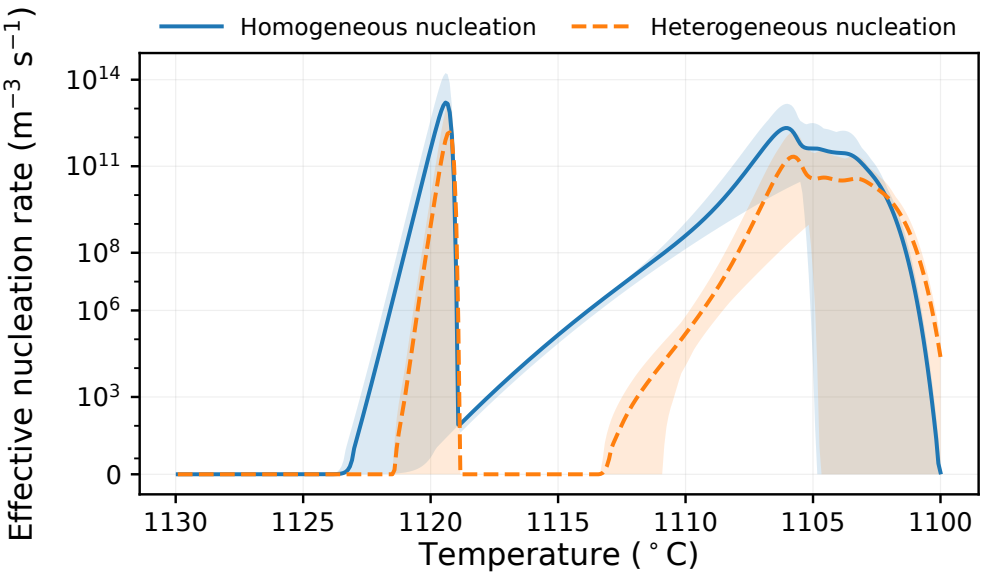


Fig. 2 Effective homogeneous and heterogeneous plagioclase nucleation rates as a function of temperature for the Iezzi et al. benchmark calculations. Because homogeneous and heterogeneous nucleation are intrinsically expressed with different dimensional rates, J_{hom} [$\mathrm{m^{-3}\,s^{-1}}$] and J^{A}_{het} [$\mathrm{m^{-2}\,s^{-1}}$], respectively, both mechanisms are converted to an equivalent volumetric rate to allow direct comparison. For each timestep, the effective rates are calculated as

$$J^{\mathrm{eff}}_{\mathrm{hom}} = \frac{\sum_e \lambda_{\mathrm{hom},e}}{\Delta t \sum_e V_e}, \qquad J^{\mathrm{eff}}_{\mathrm{het}} = \frac{\sum_e \lambda_{\mathrm{het},e}}{\Delta t \sum_e V_e},$$

where V_e is the element volume, $\lambda_{\mathrm{hom},e} = J_{\mathrm{hom},e} V_e \Delta t$ is the expected number of homogeneous nuclei, and $\lambda_{\mathrm{het},e} = J^{A}_{\mathrm{het},e} A_{\mathrm{plag},e} \Delta t$ is the expected number of heterogeneous nuclei formed on the available plagioclase surface $A_{\mathrm{plag},e}$. Thus, $J^{\mathrm{eff}}_{\mathrm{het}}$ represents the surface-controlled heterogeneous nucleation contribution expressed per unit magma volume and can be directly compared with the homogeneous contribution. The plotted quantities represent expected nucleation rates rather than the stochastic number of nuclei actually realised by Poisson sampling at each timestep. Shaded regions indicate the 2.5–97.5 percentile range among stochastic realisations, whereas the lines represent the ensemble mean.

The remaining quantities in Table 2 were not treated as free calibration parameters. The attempt frequencies were fixed at 10^{13} $\mathrm{s^{-1}}$ as atomic-scale prefactors, a_{nuc} for plagioclase was calculated from the `MELTS` molar volume, $a_{\mathrm{grow}} = 3 \times 10^{-10}$ m was adopted as a molecular jump length, and mixed diffusion–interface attachment was imposed as the kinetic formulation. The heterogeneous substrate was the dynamically resolved plagioclase surface area, so that heterogeneous nucleation increased naturally as crystal surface developed. Finally, $L/D_{\mathrm{eq}} = 2.537$ was solely a post-processing conversion used to compare the equivalent-volume model crystals with the experimentally measured long-axis CSD and did not influence the simulated crystallisation kinetics.

Table 2 Parameters adopted in the calibrated Iezzi reference model. Parameters used as calibration variables are distinguished from fixed modelling parameters and geometrical post-processing quantities. The calibration experiment corresponds to cooling at $0.5\,^{\circ}\mathrm{C\,min^{-1}}$ from 1300 to 1100 °C under air conditions. Heterogeneous nucleation parameters are effective model parameters rather than directly measured experimental quantities.

Parameter	Symbol	Plagioclase	Fe–Ti oxide
Interfacial energy	γ	$0.0445\ \mathrm{J\,m^{-2}}$	$0.46\ \mathrm{J\,m^{-2}}$
Nucleation activation energy	Q_{nuc}	$285\ \mathrm{kJ\,mol^{-1}}$	$267\ \mathrm{kJ\,mol^{-1}}$
Growth activation energy	Q_{grow}	$285\ \mathrm{kJ\,mol^{-1}}$	$267\ \mathrm{kJ\,mol^{-1}}$
Nucleation attempt frequency	ν_{nuc}	$1.0 \times 10^{13}\ \mathrm{s^{-1}}$	$1.0 \times 10^{13}\ \mathrm{s^{-1}}$
Growth attempt frequency	ν_{grow}	$1.0 \times 10^{13}\ \mathrm{s^{-1}}$	$1.0 \times 10^{13}\ \mathrm{s^{-1}}$
Nucleation structural-unit length	a_{nuc}	$(V_m/N_A)^{1/3}$	3.0×10^{-10} m
Growth jump length	a_{grow}	3.0×10^{-10} m	3.0×10^{-10} m
Attachment regime	k_{eff}	mixed diffusion–interface	mixed diffusion–interface
Heterogeneous barrier factor	ϕ_{het}	0.60	disabled
Active heterogeneous site fraction	f_{site}	0.003	disabled
Heterogeneous substrate	—	resolved plagioclase surface	none
CSD long-axis conversion	L/D_{eq}	2.537	1
Redox condition	fO_2	air	air

The 20 stochastic realisations yield a mean total crystal fraction of 12.30±1.24 vol.%, consisting of 10.72±0.98 vol.% plagioclase and 1.57±0.26 vol.% Fe–Ti oxide, in good agreement with the experimental crystallinity of 13±1 vol.%. The final plagioclase composition is also stable among realisations ($An_{70.68\pm0.93}$) and remains within the experimental range (Figure 3). In all simulations, plagioclase nucleation initiates homogeneously and is followed by heterogeneous nucleation, with homogeneous nuclei accounting for 92.48±0.28% of the final crystal number. In contrast, the absolute plagioclase population exhibited substantially larger stochastic variability, with a coefficient of variation of approximately 35%, demonstrating that stochastic nucleation primarily affects crystal number rather than final crystallised volume.

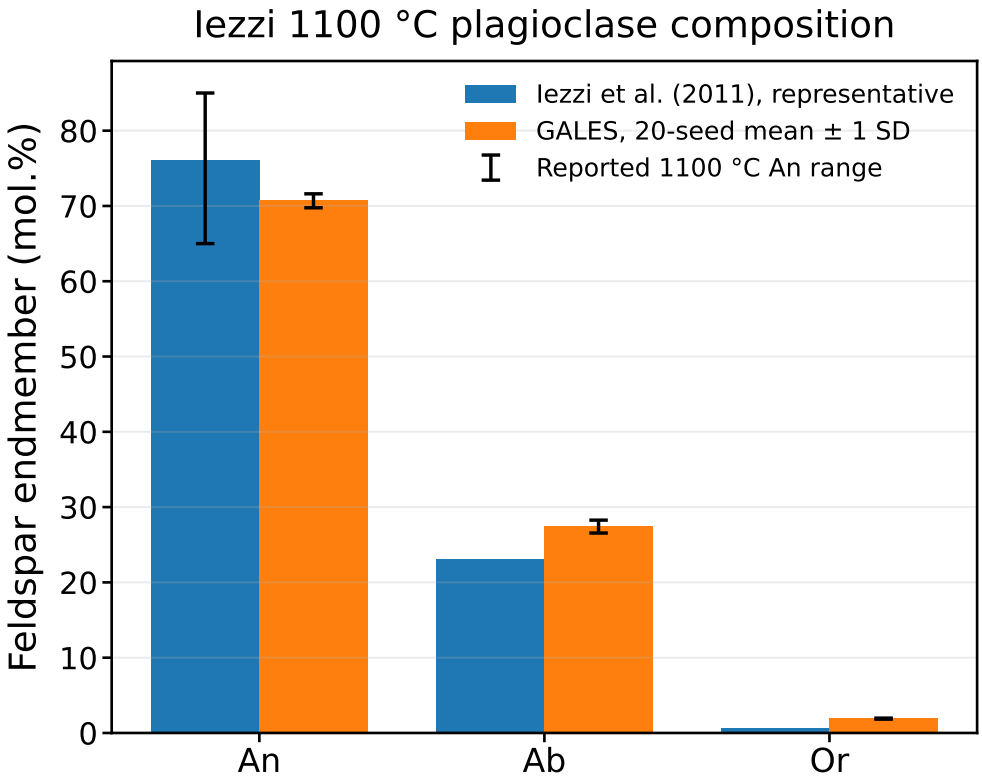


Fig. 3 Comparison between the plagioclase composition measured by Iezzi et al. (blue) and the present computations (orange).

The residual-liquid composition provides an additional independent constraint on the chemical evolution and mass balance of the model. For the experiments cooled at $0.5\,^{\circ}\mathrm{C\,min^{-1}}$ and quenched at 1100 °C, the two replicate runs of Iezzi et al. (2011) yield a pooled mean residual-glass composition of 60.18 wt.% SiO_2, 0.57 wt.% TiO_2, 16.32 wt.% Al_2O_3, 6.97 wt.% Fe_2O_3, 0.16 wt.% MnO, 3.80 wt.% MgO, 6.48 wt.% CaO, 2.79 wt.% Na_2O, 2.31 wt.% K_2O and 0.19 wt.% P_2O_5. The corresponding 20-realisation `GALES` ensemble gives 61.11±0.44 wt.% SiO_2, 0.68±0.01 wt.% TiO_2, 15.74±0.10 wt.% Al_2O_3, 6.11±0.35 wt.% $Fe_2O_3^{eq}$, 0.208±0.004 wt.% MnO, 4.33±0.01 wt.% MgO, 7.02±0.04 wt.% CaO, 2.45±0.00 wt.% Na_2O, 2.24±0.03 wt.% K_2O and 0.173±0.003 wt.% P_2O_5 (Figure 4). The model therefore reproduces the first-order residual-melt composition and direction of chemical evolution, although systematic oxide-specific offsets remain. In particular, the calculated melt is systematically richer in SiO_2, MgO and CaO and poorer in Al_2O_3, total Fe and Na_2O than the experimental glass. The overall compositional RMSE is approximately 0.51 wt.%. Because the inter-realisation variability is small relative to most of these model experiment differences, the residual-liquid discrepancies are predominantly systematic rather than a

consequence of stochastic nucleation. For consistency with Iezzi et al., who report all iron as Fe_2O_3, the modelled FeO and Fe_2O_3 contributions are combined and expressed as Fe_2O_3-equivalent.

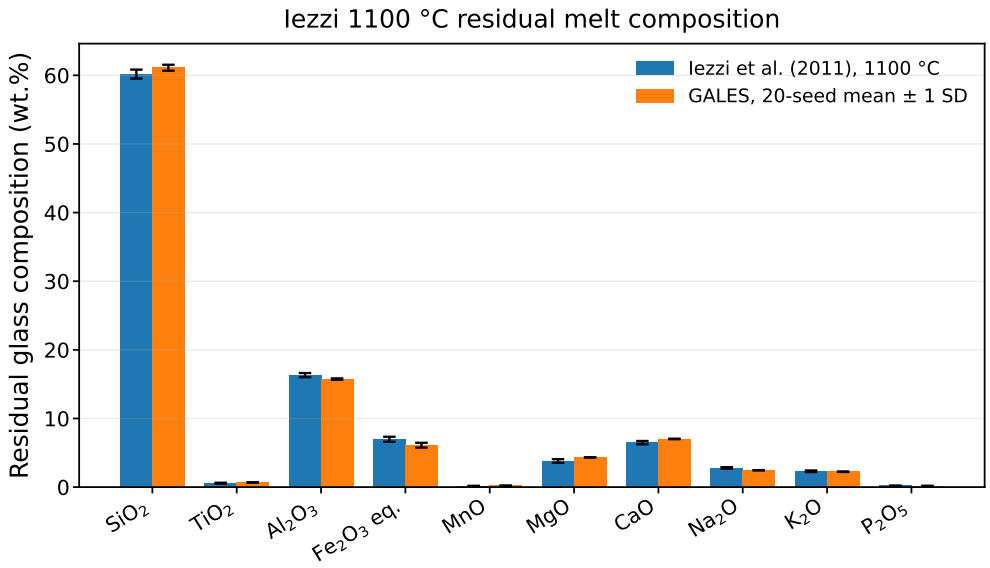


Fig. 4 Comparison between the residual melt composition measured by Iezzi et al. (blue) and the present computations (orange).

The crystal-size distribution provides a more stringent test of the coupled nucleation–growth history. The experimental CSD of Iezzi et al. (2011) for the $0.5\,^{\circ}\mathrm{C\,min^{-1}}$, $1100\,^{\circ}\mathrm{C}$ run was digitized from their Fig. 8 and compared with the 20-realisation `GALES` ensemble after conversion of the modelled equivalent-volume diameter to the experimental long-axis dimension using $L/D_{\mathrm{eq}} = 2.537$ (Figure 5). Because the absolute normalisation of the digitized experimental CSD is uncertain, the comparison is performed primarily on CSD shape after applying a constant vertical offset to the modelled distribution. The comparison therefore evaluates the distribution of crystal sizes but is not used to validate the absolute crystal number density. The model reproduces the presence of a dominant population of small to intermediate plagioclase crystals, but the simulated distribution is systematically narrower than the experimental one and does not reproduce the coarse-crystal tail. The mean maximum modelled long axis is 109.9 ± 6.9 μm, whereas the experimental population extends to approximately 200 μm. The ensemble comparison further shows that crystals in the 146.8 μm size class occur in only one of the 20 stochastic realisations, while no modelled crystals populate the 215–316 μm classes. The limited spread among stochastic realisations relative to the model–experiment discrepancy indicates that the missing coarse-crystal population is systematic rather than a consequence of random nucleation sampling. This suggests that the present nucleation–growth formulation captures

the first-order crystal population but underestimates the processes responsible for the development of the large-size tail, such as prolonged growth, coarsening, agglomeration, or crystal–crystal interactions, all of which are observed experimentally but are not explicitly represented in the present model.

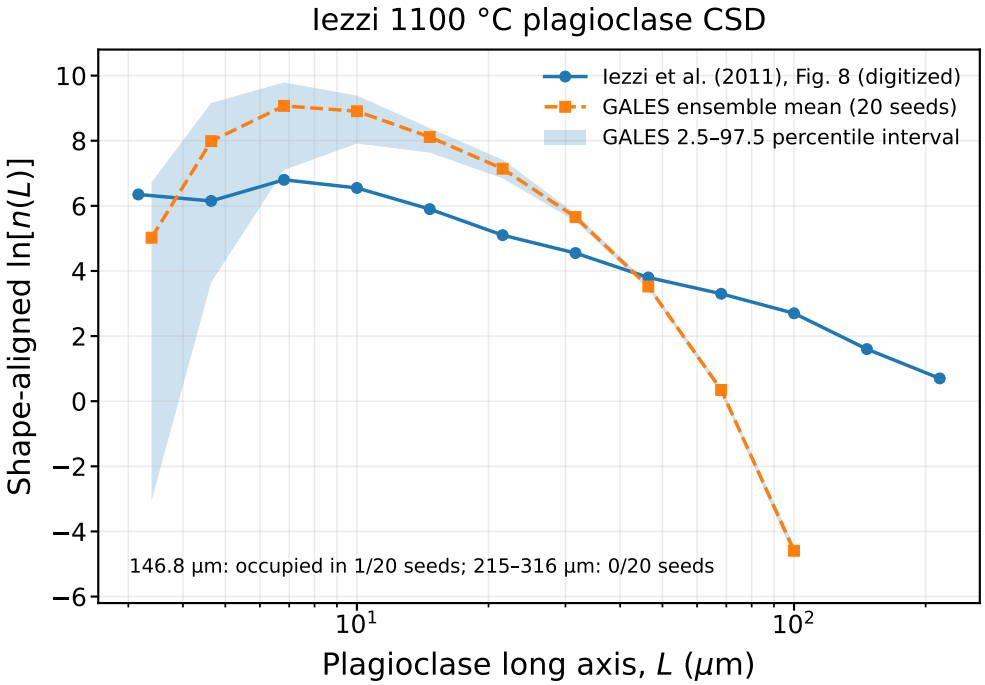


Fig. 5 Shape comparison between the plagioclase CSD digitized from Iezzi et al. (2011, Fig. 8) and the GALES 20-realisation ensemble at 1100 °C. Modelled equivalent-volume diameters are converted to long-axis dimensions using $L/D_{\mathrm{eq}} = 2.537$. A constant vertical offset is applied for shape comparison; the shaded region represents the 2.5th–97.5th percentile interval among stochastic realisations.

5.2 Billon et al. experiment

Billon et al. (2025) was selected as a second benchmark because it provides an unusually comprehensive experimental characterization of plagioclase crystallisation in a natural basaltic andesite, including phase abundance, crystal number density, three-dimensional morphology, crystal-size distributions, and independently derived nucleation and growth rates. The experiments also explore much slower cooling conditions and a different melt composition and redox state than the Iezzi calibration, thereby providing a stringent test of the transferability of the model. An important difference with the Iezzi experiment is that the starting state of the Billon cooling experiments was not crystal-free. After the 1190 °C pre-treatment, a small population of inherited plagioclase crystals remained in the charge. These pre-existing crystals were therefore included explicitly in the numerical initial condition and provided both

an initial crystal population for subsequent growth and available surface area for heterogeneous nucleation. Among the Billon experiments, run G2-2 was selected. This charge was cooled from the 1190 °C post-treatment state to 1140 °C at 3 °C/h and contains approximately 11 vol.% plagioclase at the final quench temperature, with no Fe–Ti oxide or pyroxene. The run therefore provides a well-developed crystal population and CSD while remaining sufficiently simple to isolate plagioclase nucleation and growth. Experiments quenched closer to the liquidus contain very small and highly variable crystal populations, whereas lower-temperature experiments progressively introduce additional crystalline phases and greater textural complexity. G2-2 therefore represents a compromise between statistical robustness of the crystal population and simplicity of the phase assemblage.

Starting from the calibration obtained for the Iezzi et al. experiments, only a limited recalibration was required for the Billon et al. benchmark. The homogeneous CNT and growth parameters were retained unchanged, whereas the effective heterogeneous nucleation parameters were recalibrated to account for the fundamentally different, inherited-seed-dominated initial condition (Table 3).

The heterogeneous nucleation parameters were explored using a 6×5 sensitivity grid in ϕ_{het} and f_{site}. The same random-number seed was used for all 30 simulations in order to isolate the effect of parameter changes from stochastic variability. The grid revealed a clear trade-off between the heterogeneous barrier reduction factor and the active-site fraction. The pair

$$\phi_{\mathrm{het}} = 3.3 \times 10^{-4}, \qquad f_{\mathrm{site}} = 2.5 \times 10^{-5}$$

was selected because it provided was selected because it reproduced the experimental crystal number density while providing the lowest CSD mismatch among the explored parameter pairs and remaining away from the boundaries of the parameter space. Across the sensitivity grid, the final crystal number density varies strongly, whereas the final plagioclase volume fraction changes only weakly. The residual-liquid composition is also nearly insensitive to ϕ_{het} and f_{site}. This behaviour reflects a nucleation-growth compensation. Larger nucleation rates generate a greater number of crystals, so the crystallised mass is distributed among more individual grains. Conversely, lower nucleation rates produce fewer crystals, which can undergo greater individual growth. As a result, substantially different crystal populations can develop while producing similar total crystallised masses. The final plagioclase fraction is therefore not imposed directly by the thermodynamic calculation. Thermodynamics determines the instantaneous driving force for crystallisation and the composition of the incipient solid, whereas the actual amount of material transferred from the liquid to the crystal population is controlled kinetically by the coupled evolution of nucleation and growth. The weak dependence of the final plagioclase fraction on ϕ_{het} and f_{site}, despite large variations in N_V, should therefore not be interpreted as evidence that the crystallised mass is thermodynamically fixed. Rather, it is an emergent property of the coupled nucleation-growth system. In this sense, the pair $(\phi_{\mathrm{het}}, f_{\mathrm{site}})$ primarily controls the number of crystals produced and the resulting crystal-size distribution, whereas the thermodynamic trajectory largely controls the evolution of the residual melt and the

Table 3 Parameters adopted for the Billon et al. G2-2 benchmark. The plagioclase homogeneous-nucleation and growth parameters were transferred from the Iezzi et al. calibration. Only the heterogeneous nucleation parameters ϕ_{het} and f_{site} were recalibrated against the Billon experiment.

Parameter	Symbol	Plagioclase	Status / main constraint
Interfacial energy	γ	0.0445 J m^{-2}	transferred from Iezzi
Nucleation activation energy	Q_{nuc}	285 kJ mol^{-1}	transferred from Iezzi
Growth activation energy	Q_{grow}	285 kJ mol^{-1}	transferred from Iezzi
Nucleation attempt frequency	ν_{nuc}	1.0×10^{13} s^{-1}	fixed prefactor
Growth attempt frequency	ν_{grow}	1.0×10^{13} s^{-1}	fixed prefactor
Nucleation structural-unit length	a_{nuc}	$(V_m/N_A)^{1/3}$	computed from `MELTS`
Growth jump length	a_{grow}	3.0×10^{-10} m	fixed molecular scale
Attachment regime	k_{eff}	mixed diffusion–interface	transferred formulation
Heterogeneous barrier factor	ϕ_{het}	3.3×10^{-4}	N_V, nucleation window, CSD
Active heterogeneous site fraction	f_{site}	2.5×10^{-5}	N_V, J_{batch}, CSD
Heterogeneous substrate	–	resolved plagioclase surface	physical model
Initial seed fraction	ϕ_{seed}	0.00321	GERO-0 experiment
Initial seed number density	$N_{V,0}$	1.98×10^{12} m^{-3}	GERO-0 experiment
`MELTS` model	–	`Rhyolite-MELTS 1.2.0` (mode 4)	Billon thermodynamic model
Redox condition	fO_2	NNO	experimental condition

composition of the incipient plagioclase. The sensitivity analysis thus shows that similar final crystal fractions can arise from markedly different crystallisation histories. The resulting heterogeneous nucleation rates are shown in Figure 6.

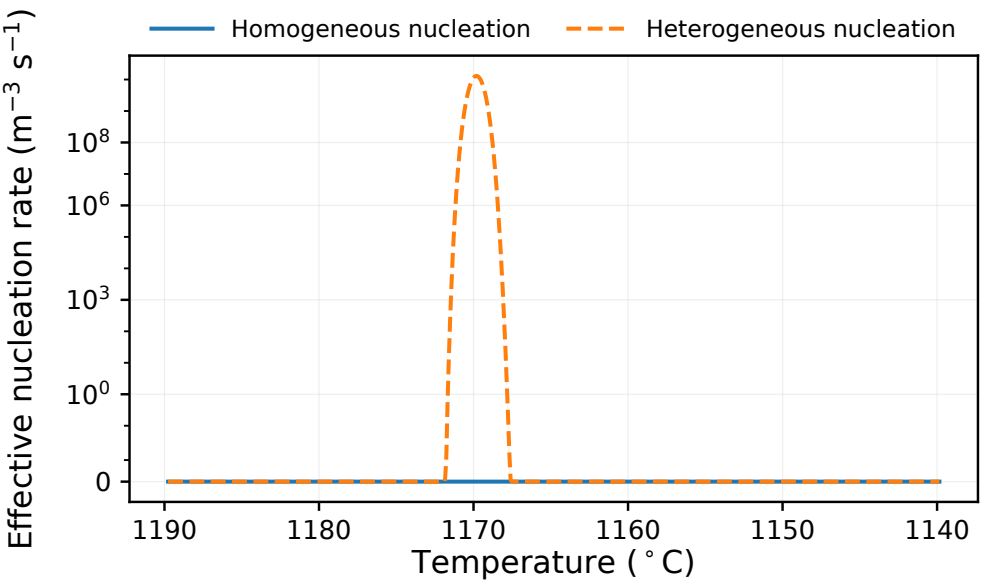


Fig. 6 Effective homogeneous and heterogeneous plagioclase nucleation rates as a function of temperature for the Billon et al. benchmark calculations. Only heterogeneous nucleation is present, and its effective rate is computed as in Figure 2. The 2.5th–97.5th percentile range is imperceptible at the scale of the figure; the lines represent the ensemble mean.

To quantify the stochastic variability associated with nucleation, the final G2-2 calculation is repeated for 20 independent random-number seeds while maintaining identical thermodynamic and kinetic parameters. At 1140 °C, the simulations yield a plagioclase volume fraction of 12.3 vol.% and a crystal number density of 2×10^{13} m^{-3}, compared with experimental values of approximately 11.3 vol.% and 2.15×10^{13} m^{-3}, respectively. The corresponding batch nucleation rate is $(4.75\pm0.01)\times10^{8}$ m^{-3}s^{-1}, only about 7% lower than the experimental estimate of 5.12×10^{8} m^{-3}s^{-1}. The ensemble produces 75,320±221 new plagioclase crystals, demonstrating that both the final crystal number density and the integrated nucleation rate are essentially insensitive to the stochastic realisation. The very small standard deviations obtained for the Billon ensemble reflect the limited stochastic variability among realisations rather than an equivalent precision of the physical model or experimental constraints; consequently, they should not be interpreted as measures of the overall predictive uncertainty.

New crystal formation is strongly localized in temperature. Across the 20 realisations, nucleation begins at 1171.25±0.09 °C and ceases at 1168.65±0.09 °C, with a count-weighted mean nucleation temperature of 1169.818±0.001 °C. Thus, most new crystals formed within a temperature interval of only about 2.6 °C, corresponding to

approximately 0.87 h at the experimental cooling rate of 3 °C/h. Subsequent cooling therefore mainly promoted growth of an already established crystal population. This behaviour is qualitatively compatible with the observation by Billon et al. that nucleation and growth rates are highest close to the liquidus and subsequently decrease during cooling.

The residual-liquid composition provides an additional independent test of the thermodynamic and mass-balance treatment. At 1140 °C, the 20-seed ensemble closely reproduces the G2-2 glass composition measured by WDS. The ensemble-mean residual melt is characterised by 57.77 wt.% SiO_2, 1.45 wt.% TiO_2, 14.76 wt.% Al_2O_3, 10.80 wt.% FeO_t, 3.55 wt.% MgO, 5.89 wt.% CaO and 4.02 wt.% Na_2O, compared with experimental values of 57.83, 1.51, 15.05, 10.35, 3.39, 6.02 and 4.00 wt.%, respectively (Figure 7). Most oxide concentrations lie within one experimental standard deviation, and all are within approximately two standard deviations. The resulting compositional RMSE is only about 0.18 wt.%. This agreement indicates that the calculated degree of crystallisation and the associated chemical depletion of the melt are internally consistent with the experimental run.

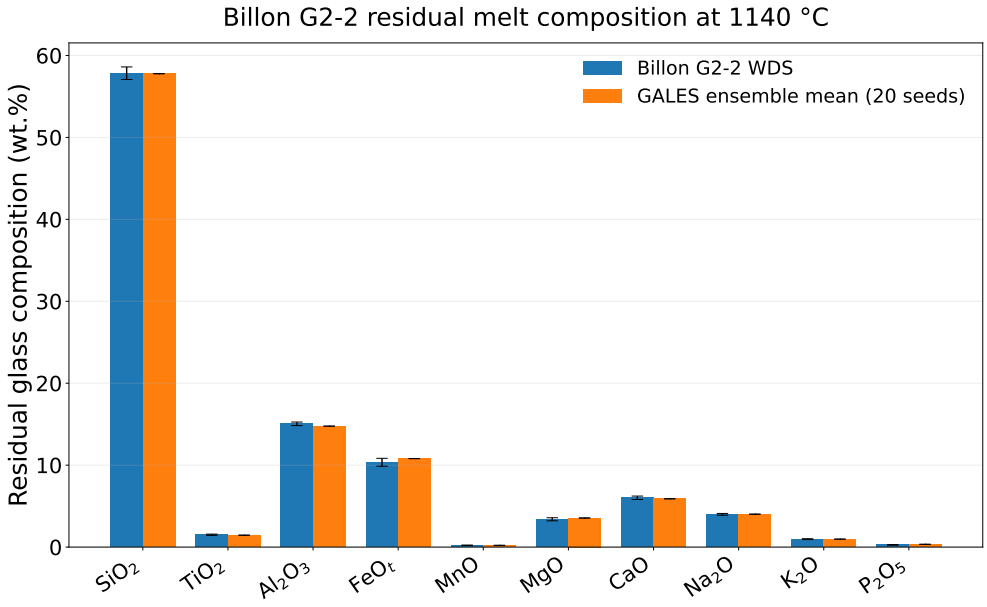


Fig. 7 Comparison between the residual melt composition measured by Billon et al. (blue) and the present computations (orange).

The agreement is less complete for plagioclase composition. The seven analysed G2-2 new-growth rims have a mean composition of $An_{59.19\pm2.39}Ab_{39.96\pm2.29}Or_{0.85\pm0.11}$, whereas the calculated incipient plagioclase at 1140°C is approximately $An_{52.45}Ab_{45.89}Or_{1.66}$. The model therefore predicts plagioclase that is about 6.7 mol.%

less anorthitic than the experimental rims (Figure 8). In contrast to the stochastic crystal-population quantities, this discrepancy is essentially identical among all 20 seeds, indicating that it is systematic rather than related to stochastic nucleation.

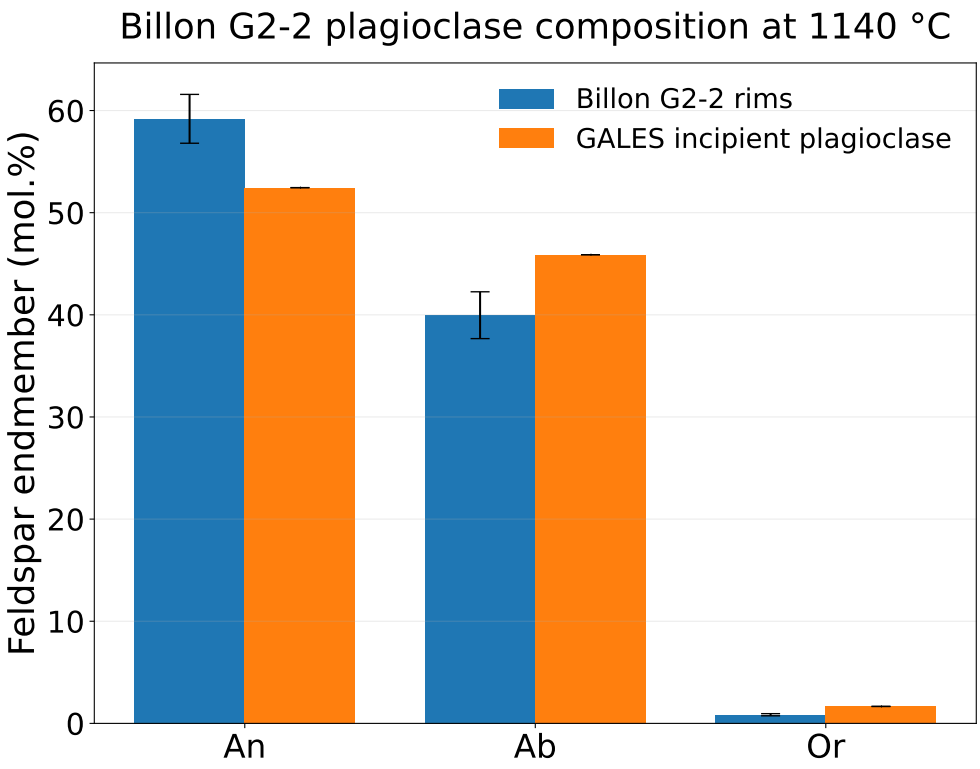


Fig. 8 Comparison between the plagioclase composition measured by Billon et al. (blue) and the present computations (orange).

Importantly, the plagioclase compositional mismatch does not appear to result primarily from an incorrect residual-liquid trajectory. The modelled G2-2 melt composition agrees closely with the measured residual glass, with an overall oxide RMSE of approximately 0.18 wt.%. Moreover, when the experimentally measured G2-2 glass is supplied directly to `Rhyolite-MELTS` at 1140 °C and NNO, the predicted plagioclase is only $An_{54.13}$, still about 5 mol.% less anorthitic than the measured rims. This suggests that the remaining discrepancy reflects, at least in part, kinetic disequilibrium in plagioclase composition or limitations in the thermodynamic description of the instantaneous feldspar composition, rather than solely an error in melt evolution.

Despite the agreement in crystal abundance and number density, the calculated crystal-size distribution differs systematically from the experimental G2-2 CSD (Figure 9). The experimental distribution spans approximately 44 to 700 μm, whereas

the modelled population occupies only the intermediate size classes between approximately 44 and 276 μm. The model particularly overestimates the population near 69 μm, while failing to reproduce both the smallest crystals and the large-size tail. Importantly, the 95% interval obtained from the 20 stochastic realisations is extremely narrow relative to the model–experiment discrepancy, demonstrating that the CSD mismatch cannot be explained by stochastic variability in crystal nucleation.

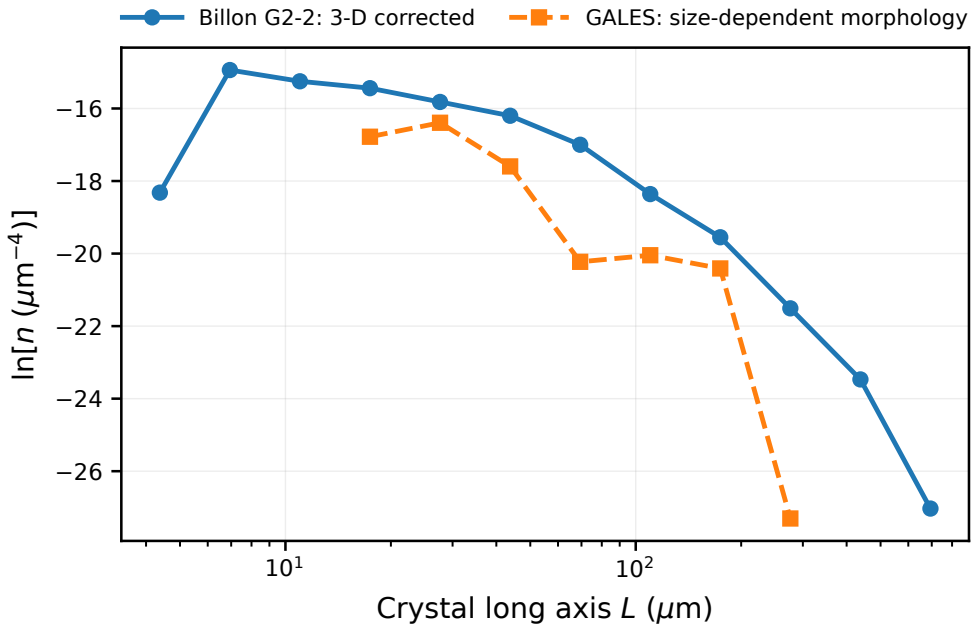


Fig. 9 Comparison between the 3-D-corrected plagioclase CSD of Billon et al. (2025) (blue) and the present calculations (orange).

6 Discussion

The two experiments constrain different parts of the model and, importantly, show why no single observable is sufficient to evaluate crystallisation kinetics. Crystal fraction mainly records total mass transfer, N_V records the accumulated number of crystals, and residual-liquid composition tests the associated chemical depletion. The CSD adds a temporal dimension because crystals with different nucleation times experience different growth histories. Agreement in one of these quantities therefore need not imply agreement in the others.

The Iezzi experiment tests the model from the onset of crystallisation. Starting from a crystal-free melt, homogeneous plagioclase nucleation develops after finite undercooling and is followed by heterogeneous nucleation as crystal surface becomes

available. The calculated total crystallinity agrees with the experiment, and the modelled plagioclase composition lies within the observed range. Residual-liquid chemistry follows the experimental differentiation trend, although the remaining oxide-specific offsets are larger than the variability among stochastic realisations. Those offsets are therefore associated with the physical or thermodynamic formulation rather than with the random sampling of nucleation. It should be emphasised that the spread among the 20 realisations quantifies only the variability arising from stochastic nucleation, because all thermodynamic, kinetic and numerical parameters are held fixed; it therefore does not represent the total uncertainty associated with parameter calibration or with the physical and thermodynamic assumptions of the model.

Texture is more restrictive. The Iezzi calculation reproduces the dominant small- to intermediate-size population, but the simulated CSD is narrower than the experimental distribution. The modelled maximum long axis is 109.9 ± 6.9 μm, compared with an experimental distribution extending to approximately 200 μm. Only one of the 20 realisations reaches the 146.8 μm size class, and none populates the larger 215–316 μm classes. The coarse tail is therefore not absent because an unfavorable stochastic realisation happened to be selected. Its persistence outside the ensemble variability instead indicates that some mechanism controlling the late evolution of crystal size is not represented by the present nucleation-growth description. Possible contributions include prolonged or heterogeneous growth histories, coarsening, aggregation and crystal–crystal interaction.

Billon provides a different test because the system already contains plagioclase when cooling begins. The Iezzi-derived interfacial energy, mixed diffusion/interface-controlled nucleation attachment kinetics and growth parameters were retained, but no homogeneous nucleation was realised during the Billon trajectory. New crystals formed exclusively through heterogeneous nucleation on the inherited and subsequently growing plagioclase surfaces. Recalibration was therefore confined to ϕ_{het} and f_{site}, which describe the efficiency and availability of heterogeneous nucleation sites.

The Billon sensitivity calculations also reveal a useful feature of the coupled model: crystal number and crystallised mass need not vary together. Substantial changes in N_V can occur while the final plagioclase fraction and residual-liquid composition change little. A larger number of nuclei divides the available crystallised mass among more crystals; a smaller number leaves more mass available for growth of each individual crystal. Final crystallinity is therefore an integrated outcome of nucleation, growth and depletion rather than a direct copy of the equilibrium phase fraction predicted by `MELTS` .

At the G2-2 endpoint, the calculated plagioclase fraction, N_V, batch nucleation rate and residual-glass composition are all close to the experimental values. Crystal composition is less well reproduced: the predicted plagioclase is more sodic than the measured new-growth rims. Supplying the measured G2-2 residual glass directly to `Rhyolite-MELTS` reduces but does not remove this difference. The melt trajectory alone therefore cannot explain the offset. Either kinetic disequilibrium during feldspar growth, limitations in the thermodynamic prediction of the instantaneous feldspar composition, or both must contribute.

The Billon CSD leads to a conclusion similar to the Iezzi comparison. Bulk crystallinity and number density can be reproduced while the observed size distribution remains broader than the calculated one. The model misses both part of the fine population and the coarse tail, and the stochastic interval is small compared with the model–experiment difference. Because the same tendency appears in two experiments with very different cooling rates, initial conditions and nucleation regimes, the discrepancy is unlikely to arise from stochastic nucleation alone or from a single poorly chosen CNT parameter.

This result is useful because it separates what is already captured from what is not. The coupled thermodynamic–kinetic formulation accounts reasonably well for the integrated mass transfer, melt differentiation and overall crystal population under both experimental conditions. The CSD, however, contains information that is not recoverable from those bulk quantities alone. In the present calculations, that missing information appears to concern the evolution of the population after nuclei have formed: variations in growth history, crystal interaction, aggregation, coarsening and morphology can alter the distribution without strongly changing final crystallinity or melt chemistry.

The comparison therefore gives the CSD a role beyond that of an additional fitting target. It acts as a diagnostic of processes that are poorly constrained by phase abundance or N_V. The present `GALES`–`MELTS` formulation provides a baseline in which thermodynamic affinity, attachment kinetics, stochastic nucleation, crystal growth and chemical depletion are coupled explicitly. Processes added in future developments can then be evaluated by asking whether they improve the crystal-scale record without degrading quantities that are already reproduced, such as crystal fraction, number density and residual-liquid chemistry.

7 Conclusions

`GALES` and `alphaMELTS` have been coupled to follow crystallisation as a time-dependent interaction between thermodynamic disequilibrium, nucleation, growth and melt depletion. `MELTS` supplies the affinity and composition of the incipient crystalline phases; `GALES` uses this information to calculate nucleation and growth and to update the crystal population. The nucleation rate combines the CNT barrier with a mixed diffusion/interface-controlled attachment prefactor, while crystal growth uses an analogous kinetic treatment. Removing the crystallised material from the liquid closes the feedback because the depleted melt determines the thermodynamic conditions for the next step.

The two experimental benchmarks exercise different parts of this formulation. In the Iezzi case, an initially crystal-free melt develops homogeneous nucleation before heterogeneous nucleation becomes important on newly created crystal surfaces. The calculation reproduces the observed crystallinity, gives plagioclase compositions within the experimental range and follows the main residual-melt differentiation trend. Billon begins instead with inherited plagioclase. Homogeneous nucleation is absent from the modelled cooling path, and all new crystals form heterogeneously. With the

Iezzi-derived interfacial energy, nucleation attachment kinetics and growth parameters retained, and only the effective heterogeneous nucleation parameters recalibrated, the calculation reproduces the final plagioclase fraction, crystal number density, batch nucleation rate and residual-glass composition. The plagioclase composition is less well reproduced, remaining systematically more sodic than the experimentally measured new-growth rims, despite the close agreement in residual-glass composition.

The CSD comparisons impose a stricter condition than these bulk observables. Both modelled distributions are narrower than their experimental counterparts even though crystallinity, N_V and melt chemistry are reasonably reproduced. The significance of this result is that those integrated quantities do not uniquely specify the crystal population. Crystal size retains information on when crystals formed, how long they grew and what happened to them after nucleation. The persistence of the CSD discrepancy across stochastic realisations also shows that it cannot be removed simply by choosing another random nucleation history.

Rather than weakening the coupled approach, this separation between successful and unsuccessful observables makes the comparison more informative. The present formulation captures much of the bulk thermodynamic, chemical and population-scale evolution while identifying the crystal-size distribution as the quantity most sensitive to physics that remains unresolved. Coarsening, aggregation, crystal interaction, morphology-dependent growth and disequilibrium crystal chemistry can therefore be introduced and tested against a model whose mass balance, melt evolution and principal nucleation behaviour are already constrained.

The resulting framework is useful not only for reproducing a crystallisation path, but for determining which observations can be explained by a given set of physical processes and which require additional mechanisms. In that sense, coupling `GALES` and `MELTS` provides a basis for progressively testing more complete descriptions of the textural and chemical evolution of magmas.

Acknowledgements. Acknowledgements are not compulsory. Where included they should be brief. Grant or contribution numbers may be acknowledged.

Author contributions. A. Longo: Conceptualization, Data curation, Formal analysis, Investigation, Methodology, Software, Validation, Visualization, Writing – original draft, Writing – review & editing. D. Garg: Conceptualization, Formal analysis, Investigation, Methodology, Software. P. Papale: Conceptualization, Formal analysis, Methodology, Funding acquisition, Project administration, Resources, Supervision.

Code availability. Crystallization computations are performed with the `GALES` code provided by (Longo et al. 2026).

Declarations

Conflict of interest. The authors declare that they have no conflicts of interest relevant to this study.

Open Access. This article is licensed under a Creative Commons Attribution 4.0 International License, which permits use, sharing, adaptation, distribution and reproduction in any medium or format, as long as you give appropriate credit to the original

author(s) and the source, provide a link to the Creative Commons licence, and indicate if changes were made. The images or other third party material in this article are included in the article's Creative Commons licence, unless indicated otherwise in a credit line to the material. If material is not included in the article's Creative Commons licence and your intended use is not permitted by statutory regulation or exceeds the permitted use, you will need to obtain permission directly from the copyright holder. To view a copy of this licence, visit https://creativecommons.org/licenses/by/4.0/.

Editorial Policies for:

Springer journals and proceedings: https://www.springer.com/gp/editorial-policies

Nature Portfolio journals: https://www.nature.com/nature-research/editorial-policies

Scientific Reports: https://www.nature.com/srep/journal-policies/editorial-policies

BMC journals: https://www.biomedcentral.com/getpublished/editorial-policies

References

Andrews BJ, Befus KS (2020) Supersaturation nucleation and growth of plagioclase: A numerical model of decompression-induced crystallization. Contributions to Mineralogy and Petrology 175:23. https://doi.org/10.1007/s00410-020-1660-9

Arzilli F, Carroll MR (2013) Crystallization kinetics of alkali feldspars in cooling and decompression-induced crystallization experiments in trachytic melt. Contributions to Mineralogy and Petrology 166:1011–1027. https://doi.org/10.1007/s00410-013-0906-1

Asimow PD, Ghiorso MS (1998) Algorithmic modifications extending MELTS to calculate subsolidus phase relations. American Mineralogist 83(9–10):1127–1132. https://doi.org/10.2138/am-1998-9-1022

Billon M, Vander Auwera J, Namur O, et al (2025) Plagioclase crystal size distributions, growth and nucleation rates in an anhydrous arc basaltic andesite. Contributions to Mineralogy and Petrology 180:26. https://doi.org/10.1007/s00410-025-02213-9

Bowen NL (1915) Crystallization-differentiation in silicate liquids. American Journal of Science 39(230):175–191. https://doi.org/10.2475/ajs.s4-39.230.175

Bowen NL (1928) The Evolution of the Igneous Rocks. Princeton University Press, Princeton

Einstein A (1905) Über die von der molekularkinetischen theorie der wärme geforderte bewegung von in ruhenden flüssigkeiten suspendierten teilchen. Annalen der Physik 322(8):549–560. https://doi.org/10.1002/andp.19053220806

Fletcher NH (1958) Size effect in heterogeneous nucleation. The Journal of Chemical Physics 29(3):572–576. https://doi.org/10.1063/1.1744540

Fokin VM, Zanotto ED, Yuritsyn NS, et al (2006) Homogeneous crystal nucleation in silicate glasses: A 40 years perspective. Journal of Non-Crystalline Solids 352(26–27):2681–2714. https://doi.org/10.1016/j.jnoncrysol.2006.02.074

Garg D, Longo A, Papale P (2018) Computation of compressible and incompressible flows with a space?time stabilized finite element method. Computers & Mathematics with Applications 75(12):4272–4285. https://doi.org/10.1016/j.camwa.2018.03.028

Ghiorso MS, Gualda GAR (2015) An H_2O–CO_2 mixed fluid saturation model compatible with Rhyolite-MELTS. Contributions to Mineralogy and Petrology 169(6):53. https://doi.org/10.1007/s00410-015-1141-8

Ghiorso MS, Sack RO (1995) Chemical mass transfer in magmatic processes IV. A revised and internally consistent thermodynamic model for the interpolation and extrapolation of liquid–solid equilibria in magmatic systems at elevated temperatures and pressures. Contributions to Mineralogy and Petrology 119(2–3):197–212. https://doi.org/10.1007/BF00307281

Giordano D, Russell JK, Dingwell DB (2008) Viscosity of magmatic liquids: A model. Earth and Planetary Science Letters 271(1):123–134. https://doi.org/10.1016/j.epsl.2008.03.038

Gualda GAR, Ghiorso MS, Lemons RV, et al (2012) Rhyolite-MELTS: A modified calibration of MELTS optimized for silica-rich, fluid-bearing magmatic systems. Journal of Petrology 53(5):875–890. https://doi.org/10.1093/petrology/egr080

Hammer JE (2004) Crystal nucleation in hydrous rhyolite: Experimental data applied to classical theory. American Mineralogist 89(11-12):1673–1679. https://doi.org/10.2138/am-2004-11-1212

Harker A (1909) The Natural History of Igneous Rocks. Methuen, London

Higgins MD (2000) Measurement of crystal size distributions. American Mineralogist 85(9):1105–1116. https://doi.org/10.2138/am-2000-8-901

Huggins EG, Ruprecht P, Ghiorso MS (2021) Using chemical affinities to understand disequilibrium textures of plagioclase preserved in magmatic systems. Geophysical Research Letters 48(10):e2021GL092884. https://doi.org/10.1029/2021GL092884

Iezzi G, Mollo S, Torresi G, et al (2011) Experimental solidification of an andesitic melt by cooling. Chemical Geology 283:261–273. https://doi.org/10.1016/j.chemgeo.2011.01.024

Kashchiev D (2000) Nucleation: Basic Theory with Applications. Butterworth-Heinemann, Oxford, https://doi.org/10.1016/B978-0-7506-4682-6.X5000-8

Kelton KF, Greer AL (2010) Nucleation in Condensed Matter: Applications in Materials and Biology. Elsevier, Oxford

Kirkpatrick RJ (1975) Crystal growth from the melt: A review. American Mineralogist 60(9–10):798–814

Kirkpatrick RJ (1981) Kinetics of crystallization of igneous rocks. In: Lasaga AC, Kirkpatrick RJ (eds) Kinetics of Geochemical Processes, Reviews in Mineralogy, vol 8. Mineralogical Society of America, p 321–398, https://doi.org/10.2138/rmg.1981.8.8

Lasaga AC (1981) Transition state theory. In: Lasaga AC, Kirkpatrick RJ (eds) Kinetics of Geochemical Processes, Reviews in Mineralogy, vol 8. Mineralogical Society of America, p 135–170, https://doi.org/10.2138/rmg.1981.8.4

Lasaga AC (1998) Kinetic Theory in the Earth Sciences. Princeton Series in Geochemistry, Princeton University Press, Princeton, New Jersey

Lindoo A, Humphreys MCS, Gordon C, et al (2025) Linking crystal shape and dynamic undercooling: a new framework for inferring magmatic crystallization histories. Contributions to Mineralogy and Petrology 180:92. https://doi.org/10.1007/s00410-025-02278-6

Longo A, Barsanti M, Cassioli A, et al (2012) A finite element Galerkin/least-squares method for computation of multicomponent compressible?incompressible flows. Computers & Fluids 67:57–71. https://doi.org/10.1016/j.compfluid.2012.07.008

Longo A, Garg D, Papale P (2026) GALES software. https://doi.org/10.5281/zenodo.23999124, URL https://doi.org/10.5281/zenodo.23999124, software

Mangler MF, Humphreys MCS, Geifman E, et al (2023) Melt diffusion-moderated crystal growth and its effect on euhedral crystal shapes. Journal of Petrology 64(8):egad054. https://doi.org/10.1093/petrology/egad054

Marsh BD (1988) Crystal size distribution (CSD) in rocks and the kinetics and dynamics of crystallization: I. theory. Contributions to Mineralogy and Petrology 99(3):277–291. https://doi.org/10.1007/BF00375362

Marsh BD (2007) Crystallization of silicate magmas deciphered using crystal size distributions. Journal of the American Ceramic Society 90:746–757. https://doi.org/10.1111/j.1551-2916.2006.01473.x

Marshall AA, Andrews BJ (2023) Modeling decompression paths in a basaltic andesite magma using the nucleation and growth of plagioclase microlites. Contributions to

Mineralogy and Petrology 178:62. https://doi.org/10.1007/s00410-023-02030-y

Muncill GE, Lasaga AC (1988) Crystal-growth kinetics of plagioclase in igneous systems: Isothermal H_2O-saturated experiments and extension of a growth model to complex silicate melts. American Mineralogist 73(9–10):982–992

Mungall JE (2002) Empirical models relating viscosity and tracer diffusion in magmatic silicate melts. Geochimica et Cosmochimica Acta 66(1):125–143. https://doi.org/10.1016/S0016-7037(01)00736-0

Musu A, Vetere F, Griffiths T, et al (2026) Experimental constraints on the impact of shear strain rate on early crystallisation dynamics and residual glass composition: Implication for magma evolution in natural systems. Journal of Petrology 67(3):egag015. https://doi.org/10.1093/petrology/egag015

Peres S, Griffiths TA, Colle F, et al (2024) Identifying crystal nucleation mechanisms in a synthetic trachybasalt: a multimodal approach. Contributions to Mineralogy and Petrology 179:84. https://doi.org/10.1007/s00410-024-02161-w

Smith PM, Asimow PD (2005) Adiabat_1ph: A new public front-end to the MELTS, pMELTS, and pHMELTS models. Geochemistry, Geophysics, Geosystems 6(2):Q02004. https://doi.org/10.1029/2004GC000816

Spillar V, Dolejš D (2013) Calculation of time-dependent nucleation and growth rates from quantitative textural data: Inversion of crystal size distribution. Journal of Petrology 54(5):913–931. https://doi.org/10.1093/petrology/egs091

Spillar V, Dolejš D (2015) Heterogeneous nucleation as the predominant mode of crystallization in natural magmas: Numerical model and implications for crystal–melt interaction. Contributions to Mineralogy and Petrology 169:4. https://doi.org/10.1007/s00410-014-1103-6

Sutherland W (1905) A dynamical theory of diffusion for non-electrolytes and the molecular mass of albumin. The London, Edinburgh, and Dublin Philosophical Magazine and Journal of Science 9:781–785. https://doi.org/10.1080/14786440509463331

Toramaru A (1991) Model of nucleation and growth of crystals in cooling magmas. Contributions to Mineralogy and Petrology 108(1-2):106–117. https://doi.org/10.1007/BF00307330

Turnbull D (1950) Kinetics of heterogeneous nucleation. The Journal of Chemical Physics 18(2):198–203. https://doi.org/10.1063/1.1747588

Turnbull D, Fisher JC (1949) Rate of nucleation in condensed systems. The Journal of Chemical Physics 17(1):71–73. https://doi.org/10.1063/1.1747055

Welsch B, Faure F, First EC (2023) Reappraising crystallization kinetics with overgrowth chronometry: an in situ study of olivine growth velocities. Journal of Petrology 64(8):egad055. https://doi.org/10.1093/petrology/egad055